

Work-hardening and ductility of artificially aged AA6060 aluminium alloy

I. Westermann^{a,b}, K.O. Pedersen^{a,c}, T. Børvik^{a,*} and O.S. Hopperstad^a

^a *Structural Impact Laboratory (SIMLab), Department of Structural Engineering, Norwegian University of Science and Technology, NO-7491 Trondheim, Norway*

^b *Department of Materials Science and Engineering, Norwegian University of Science and Technology, NO-7491 Trondheim, Norway*

^c *SINTEF Materials & Chemistry, NO-7465 Trondheim, Norway*

Abstract

The work-hardening and ductility of an artificially aged AA6060 aluminium alloy were studied based on tensile tests of smooth and notched cylindrical samples. The alloy was tested after three processing steps, each followed by artificial aging. These processing steps were casting and homogenization, extrusion, and cold rolling and heat treatment to obtain a recrystallized grain structure. Subsequent to each of these processing steps, the material was tested after artificial aging to underaged, peak aged and overaged conditions. The true stress-strain curve to failure was determined by use of a laser-based measurement system. The Bridgman correction was applied to estimate the equivalent stress-strain curves, and the work-hardening behaviour was analysed using an extended Voce approach. Fractography was applied to study the failure mechanisms for material exposed to the different processing steps and temper treatments. To evaluate the use of the Bridgman correction and to study the notch strengthening effect observed experimentally, finite element simulations were performed using the Gurson model. By comparing the three processing steps, the effects of the texture on the strength and work-hardening were obtained experimentally for the three tempers. The effect of particle size, shape and distribution on the failure strain was observed.

Keywords: Aluminium alloy; work-hardening; fracture mechanisms; scanning electron microscopy; fractography

* Corresponding author.

Telephone: + 47-73-59-46-47; e-mail address: tore.borvik@ntnu.no

1. Introduction

Age-hardened AlMgSi alloys are often used in safety components of automotive vehicles. In such applications, the energy absorption of the structural component is a design criterion and depends on the yield strength, work-hardening and ductility of the alloy. Work-hardening has twofold effect as it increases the force level and contributes to spreading the plasticity over a larger part of the structure, thus increasing the robustness of the structure.

The strength and work-hardening of heat-treatable aluminium alloys, like the AlMgSi alloys, are determined primarily by elements in solid solution and clusters/GP-zones if the alloy is naturally aged at room temperature. If the alloy is artificially aged at elevated temperature, a high density of hardening precipitates plays a major role (Myhr et al., 2010). Since atoms in solid solution and clusters/GP-zones effectively reduces dynamic recovery, i.e., the annihilation and recovery of stored dislocations, naturally aged alloys tend to exhibit lower strength but higher work-hardening than artificially aged alloys, where a large part of the solute atoms precipitate to hardening particles (Cheng et al., 2003; Embury et al., 2006). While small coherent precipitates are sheared by moving dislocations, larger incoherent precipitates are bypassed by creation of geometrically necessary dislocations, thus contributing to the work-hardening (Ashby, 1970). An artificially aged aluminium alloy will, depending on the aging time and aging temperature, to various degrees contain atoms in solid solution, shearable and non-shearable precipitates, which affect the strength, work-hardening and ductility of the material (Johnsen et al., 2013). The ductility of artificially aged aluminium alloys is known to depend on several aspects: primary particles (amount, size, shape and distribution); intergranular precipitation and precipitate free zones in the vicinity of the grain boundaries; the plastic behaviour of the grain; and crystallographic and morphological texture produced by the forming process (Dumont et al., 2003). The physical mechanisms responsible for ductile failure of metallic materials are nucleation, growth and coalescence of voids (e.g. Teirlinck et al., 1988; Benzerga and Leblond, 2010). The voids nucleate at constituent particles or inclusions either by particle cracking or particle-matrix decohesion (Maire et al., 2011) or they may pre-exist in the material (Toda et al., 2014). Void coalescence is caused by localized plastic deformation and necking of the ligament between adjacent voids, while if the material contains two classes of particles of different size and spacing, void-sheet formation may take place and lead to shear fracture (Teirlinck et al., 1988). Previous studies have indicated that the tensile failure strain of aluminium alloys scales with the yield strength for a constant microstructure (see e.g. Lloyd, 2003; Liu et al., 2011, Westermann et al., 2014;

Pedersen et al., 2015). By constant microstructure it is meant here that the microstructural strengthening and fracture mechanisms remain essentially the same between the alloys showing this scaling rule (Lloyd, 2003).

In previous papers by the authors, the influence of microstructure on the strength, work-hardening and ductile fracture of several aluminium alloys have been studied (Westermann et al., 2014; Pedersen et al., 2015). However, the effect of artificial aging was not investigated in these studies. In the present paper, yield strength, work-hardening and tensile ductility of an AA6060 aluminium alloy are reported for different combinations of forming process (or thermo-mechanical processing) and artificial aging time. Using a laser-based measurement system and the Bridgman correction, the equivalent stress-strain curves up to failure were estimated. Notched tensile specimens were also tested to investigate the effect of higher stress triaxiality on the ductility. The alloy was tested in uniaxial tension after three different processing steps (i.e., casting and homogenization, extrusion, and cold rolling and recrystallization) followed by artificial aging to three different tempers (i.e., underaged, peak aged and overaged conditions). The initial microstructure of the alloy was characterized by use of optical and scanning electron microscopy, and fractography was applied to study failure mechanisms for the different temper conditions. Finite element (FE) simulations of the smooth and notched samples with the Gurson model were used to check the accuracy of the Bridgman correction and to examine the notch-strengthening effect observed experimentally.

Subsequent to casting and homogenization, the AA6060 alloy has random texture, while the primary particles, which are large and have complex shapes, are situated at the grain and dendrite boundaries. After the extrusion process, the alloy is strongly textured, showing an intense recrystallization texture, and the primary particles are broken-up and aligned along the rolling direction. Subsequently cold cross-rolling with ensuing heat treatment and recrystallization of the extruded material was done to obtain nearly random texture, while to a large extent retaining the particle distribution. Thus, by comparing these three processing routes evidence of the influence of the texture on the strength and work-hardening and the particle size, shape and distribution on the failure strain is obtained experimentally for the three tempers.

2. Materials

The aluminium alloy AA6060 was provided as DC cast extrusion ingots of 100 mm diameter produced in a laboratory casting machine by Hydro Aluminium R&D Sunndal. The chemical composition in wt% is 0.2 Fe, 0.5 Mg, 0.4 Si and Al balance.

The three subsequent processing steps of the alloy were 1) casting and homogenization, 2) extrusion, and 3) cold rolling and heat treatment to obtain a recrystallized grain structure.

The homogenization was carried out in a laboratory furnace with heating rate 100 °C/h, holding temperature 585 °C, holding time 2.5 h, and cooling rate to room temperature 300 °C/h. The temperature-time cycle is similar to a typical industrial practice and consists of a soaking treatment followed by a predetermined cooling rate. The material processing steps subsequent to casting is illustrated in Figure 1.

The ingots were further extruded in an 800 tons laboratory press to rectangular shaped profiles with dimensions 10 mm × 50 mm for investigation of step 2) and 20 mm × 25 mm for further processing in step 3), using industrial relevant extrusion parameters, i.e., billet temperature of 475°C, container temperature of 435°C and ram speed of 5 mm/s. The profiles were cooled in air.

The final processing route, i.e., step 3), was obtained by giving the 20 mm × 25 mm profile a solid solution heat treatment at 540°C for 30 min, followed by water quenching. Then the profile was cold cross-rolled to dimension 12 mm × 12 mm in a laboratory rolling mill, prior to a solution heat treatment at 500°C for 5 min (the low temperature was used to prevent abnormal grain growth, but it is still above the solvus line) and water quenching to achieve a recrystallized grain structure with a texture close to random. A similar method was used by Furu and Pedersen (2006).

After each processing step (1, 2 and 3) the material was tested after solution heat treatment (540°C for 15 min for step 1 and 2, and the above mentioned recrystallization procedure of 500°C for 5 min for step 3) and subsequent artificial ageing at 175°C for 2 hours, 8 hours and 11 days—thus obtaining underaged, peak aged and overaged conditions. The resulting tempers will be denoted T6x, T6 and T7, respectively, while the materials obtained after the three processing routes were named: 1) cast and homogenized (CH), 2) extruded (EX) and 3) rolled and recrystallized (RR)—and these abbreviations will be used henceforth.

3. Experimental procedures

3.1 Mechanical testing

Triplicate quasi-static tensile tests were performed on smooth and notched cylindrical samples respectively oriented along the longitudinal axis of the cast ingot. The smooth samples had 6 mm diameter and 40 mm parallel length, while the notched samples had 6 mm minimum diameter and notch radius equal to 2.0 mm. The applied force and the diameter of the specimen's minimum cross-section were measured continuously until fracture. The latter was made possible using an in-house measuring rig with two perpendicular lasers that accurately measured the specimen diameter (Fourmeau et al., 2013). Based on these measurements the true stress $\sigma = F/A$ and the true strain $\varepsilon = \ln(A_0/A)$ were calculated, where F is the applied force, $A_0 = \frac{\pi}{4}D_0^2$ is the initial cross-section area, and D_0 is the initial diameter of the gauge section. The current area was estimated as $A = \frac{\pi}{4}D_1D_2$, where D_1 and D_2 are the measured diameters of the presumed elliptic shape of the cross-section. Assuming orthotropic symmetry of the extruded and rolled materials, D_1 and D_2 are measured along the transverse principal axes of anisotropy. The failure strain is defined as $\varepsilon_f = \ln(A_0/A_f)$, where A_f is the measured minimum cross-section area at maximum true stress. It should be noted here that the true stress and the true strain measured within the diffuse neck or notch are average values over the minimum cross-section.

To estimate the equivalent stress-strain curves after the onset of necking, the Bridgman correction is used for the smooth samples. The equivalent stress is accordingly expressed as (Bridgman, 1944)

$$\sigma_{eq} = \frac{\sigma}{(1 + 2R/a) \cdot \ln(1 + a/2R)} \quad (1)$$

where a is the minimum radius and R is the radius of curvature of the neck. The neck geometry was approximated by the relation proposed by Le Roy et al. (1981)

$$\frac{a}{R} = k(\varepsilon^p - \varepsilon_u^p) \quad (2)$$

where $\varepsilon^p = \varepsilon - \sigma/E$ is the logarithmic plastic strain, E is the elastic modulus, ε_u^p is the value of ε^p at incipient necking and k is an empirical parameter. Le Roy et al. (1981) used $k = 1.11$ and this value was adopted for all materials in this study. While the CH and RR

materials are practically isotropic, the EX materials exhibit marked plastic anisotropy, which implies that the use of the Bridgman correction becomes more uncertain.

It is possible to assess the accuracy of the Bridgman correction for textured materials using an anisotropic plasticity model. This was done by Khadyko et al. (2014) for the extruded alloys AA6060 and AA6082 in temper T4. The Bridgman correction over- or underestimated the equivalent stress depending on the plastic anisotropy of the material. But compared with the true stress-strain curves, the Bridgman-corrected stress-strain curves were in reasonable agreement with the equivalent stress-strain curves obtained with the anisotropic plasticity model. While numerical simulations with an anisotropic plasticity model were outside the scope of the present study, finite element simulations of the tensile tests on the RR materials were conducted using the Gurson model. The aim was to check the accuracy of the Bridgman correction as defined by Equations (1) and (2), and further to analyse the notch-strengthening effect observed in the experiments. The results from the numerical simulations will be presented in Section 5.3.

To describe and analyse the work-hardening of the materials, the Bridgman-corrected stress-strain curves from the tests on the smooth samples were represented by a two-term Voce hardening rule

$$\sigma_{eq} = \sigma_0 + R, \quad R = \sum_{i=1}^2 Q_i \left(1 - \exp(-C_i \varepsilon^p)\right) \quad (3)$$

where σ_0 is the yield stress and R is the work-hardening, which is governed by the constants Q_i and C_i , $i = 1, 2$. The hardening modulus θ is defined as

$$\theta \equiv \frac{dR}{d\varepsilon^p} = \sum_{i=1}^2 \theta_i \exp(-C_i \varepsilon^p) \quad (4)$$

where the moduli $\theta_i \equiv C_i Q_i$ represent the contributions to the initial work-hardening modulus from the two hardening terms. Thus $\theta_1 + \theta_2$ is the initial work-hardening modulus in absence of dynamic recovery (Lloyd, 2006). The parameters Q_i define the saturation values of the two hardening terms, and the saturation stress obtained at large strain is $\sigma_{sat} = \sigma_0 + Q_1 + Q_2$. The parameters C_i determine how fast the two hardening terms approach their saturation values and govern the rate of dynamic recovery. We will arrange the hardening terms so that $C_1 \geq C_2$ which implies that the first term will always saturate at a lower strain than the second term. Since $C_1 \geq C_2$ for all combinations of material and temper in the present study, the first

hardening term is important for the work-hardening at low and moderate strains (stage III), while the second hardening term controls the work-hardening at large strains (stage IV).

3.2 Microstructure characterisation

Samples of all three materials (one alloy, three processing routes) were mechanically ground and polished followed by electro polishing. The distribution of the constituent particles was obtained by image processing of back scattered electron (BSE) micrographs taken in a Hitachi SU-6600 FESEM operated at 5.0 kV. The polished specimens were also anodized at room temperature for 2 min using HBF_4 to reveal the grain structure under polarized light in the optical microscope.

The crystallographic texture of the materials was determined by the electron back-scatter diffraction (EBSD) technique in the Hitachi SU-6600 FESEM operated at 20 kV. The EBSD measurements were done in a random plane for the CH material, in the ED/ND plane for the EX and RD material. Here, ND is the normal (through-thickness) direction and TD is the transverse direction of the profile. A step size of 5 μm was applied and between 800 and 2000 grains were measured. The orientation distribution functions (ODF) were calculated by the EDAX TSL OIM software, using a harmonic series expansion and average grain orientation weighted by the grain size in the calculations. Triclinic sample symmetry was assumed for the CH and RR materials and orthotropic sample symmetry for the EX material. The texture measurements were performed before artificial aging and assumed to be independent of the succeeding aging process.

Fracture surfaces of the failed tensile tests were investigated in a Zeiss Gemini Supra 55 VP FESEM operated at 10 kV.

4. Finite element modelling

A numerical study was performed to evaluate the accuracy of the Bridgman-correction used to obtain the equivalent stress-strain curves of the materials and to examine the notch-strengthening effect. Finite element simulations of the tensile tests on smooth and notched samples were conducted to determine the stress-strain behaviour of the RR materials for large strains. The RR materials were selected because they exhibit nearly isotropic behaviour and high ductility. The numerical simulations were carried out using the explicit solver of the finite element code LS-DYNA (www.lstc.com, 2013). Axisymmetric four-node quadrilateral elements with one-point quadrature were used to mesh the smooth and notched tensile samples, employing stiffness-based hourglass control to avoid zero-energy modes. Based on

previous numerical studies by Westermann et al. (2014), 20 elements were applied across the radius for both the smooth and notched samples, giving a characteristic element size of 0.15 mm in the gauge area. Mass scaling was used to reduce the computation time, and it was checked that the kinetic energy remained negligible compared with the internal energy of the samples during the deformation process.

The behaviour of the RR materials was described using the Gurson model (Gurson, 1977). The Gurson yield criterion is defined as (Tvergaard, 1981)

$$\Phi = \frac{\sigma_{eq}^2}{\sigma_M^2} + 2fq_1 \cosh\left(\frac{q_2 \text{tr}\boldsymbol{\sigma}}{2\sigma_M}\right) - (1 + q_3 f^2) = 0 \quad (5)$$

where $\sigma_{eq} = \sqrt{\frac{3}{2}\boldsymbol{\sigma}' : \boldsymbol{\sigma}'}$ is the von Mises equivalent stress, $\boldsymbol{\sigma}'$ being the deviatoric part of the Cauchy stress tensor $\boldsymbol{\sigma}$, and f is the void volume fraction. The parameters q_1 , q_2 and q_3 were given the values $q_1 = 1.5$, $q_2 = 1$ and $q_3 = q_1^2$ suggested by Tvergaard (1981). The flow stress of the matrix material, σ_M , is defined by the two-term Voce relation (cf. Equation (3))

$$\sigma_M = \sigma_0 + \sum_{i=1}^2 Q_i (1 - \exp(-C_i \varepsilon_M)) \quad (6)$$

where ε_M is the plastic strain of the matrix material, defined from the plastic power as

$$\boldsymbol{\sigma} : \mathbf{D}^p = (1 - f) \sigma_M \dot{\varepsilon}_M \quad (7)$$

The plastic rate-of-deformation tensor \mathbf{D}^p is defined by the associated flow rule. The void growth relation is expressed as

$$\dot{f} = (1 - f) \text{tr}\mathbf{D}^p \quad (8)$$

A continuum model for void nucleation was introduced in the Gurson model by Chu and Needleman (1980) and has later been used extensively, e.g. by Chen et al. (2005) in a study on the stretch flange forming of aluminium alloy sheets. Owing to the lack of quantitative data, void nucleation was neglected in the simulations conducted here, and the single parameter of the Gurson model, in addition to the hardening parameters, is then the initial void volume fraction f_0 . A similar approximation was employed by Xue et al. (2010) when addressing calibration procedures for the modified Gurson model of Nahshon and Hutchinson (2008).

It is here assumed that the voids have minor influence on the work-hardening at stress triaxialities occurring during the uniaxial tensile test (Xue et al., 2010). This means that the

yield stress and hardening parameters obtained by the Bridgman correction can be used for the matrix material, and f_0 is the only additional parameter that needs to be calibrated. It was shown by Westermann et al. (2014) that this is a reasonable assumption for sufficiently small values of f_0 . No attempt was made here to link the value of f_0 to the volume fraction of particles in the materials. As the material has lost all its strength when f equals $1/q_1$ (e.g. Tvergaard and Needleman, 1984), the elements were eroded as f reached 90% of this critical value to avoid numerical problems.

5. Results and discussion

5.1 Initial microstructure

The grain structure, the particle distribution and the crystallographic texture of the materials are presented in Figure 2. These results were obtained by Pedersen et al. (2015) for the CH, EX and RR materials after natural aging to a stable condition. However, the grain structure, the primary particle distribution as well as the crystallographic texture remain unaltered by the artificial aging treatment applied here, and the results are therefore valid also for the underaged, peak aged and overaged conditions.

The average spherical grain size was obtained from the EBSD data, where a misorientation of 15° was used to define the high-angle grain boundary, and was found to be $66\ \mu\text{m}$, $59\ \mu\text{m}$ and $43\ \mu\text{m}$ for the CH, EX and RR materials, respectively.

The CH material had equiaxed grain structure and an inhomogeneous distribution of the constituent particles. These particles are mainly located to the grain and dendrite boundaries. A recrystallized grain structure was obtained by the extrusion, and the constituent particles were broken-up and aligned in stringers along the extrusion direction, giving more evenly distributed particles in the matrix compared to the CH material. This feature became even more pronounced after cold rolling and recrystallization.

As expected, the CH material exhibited almost random texture with maximum intensity less than 3, which was also the case for the RR material, albeit the maximum intensity was slightly higher (see Figure 2). On the contrary, the EX material had strong texture with maximum intensity about 116; the main texture component being cube (44%).

5.2 Stress-strain curves

The mechanical data obtained from the tensile tests on the smooth specimens are compiled in Table 1, which gives the 0.2% yield stress, $\sigma_{0.2}$, the true stress at necking, σ_u , the true strain

at necking, ε_u , the maximum true stress, σ_f , and the true strain at maximum true stress, ε_f . Table 2 presents the parameters of the two-term Voce hardening rule in Equation (3), which was found to provide excellent agreement with representative Bridgman-corrected stress-strain curves calculated from Equations (1) and (2).

Measured true stress-strain curves up to failure for smooth and notched samples for all materials and tempers are plotted in Figure 3. The failure strain is here defined as the true strain at maximum true stress, which is assumed to occur at void coalescence. Results for three repeat tests are included to demonstrate the scatter between the repetitions. With some exceptions, the repeatability between parallel tests was good, both with respect to stress level and strain to failure. It becomes apparent from these plots that there is a strong influence of the notch—and thus the stress triaxiality—on the tensile failure strain, which also depends on the forming process and the artificial aging time. In particular, the decrease in failure strain with increased stress triaxiality is more pronounced for tempers T6 and T7 than for the softer temper T6x. We will see below that this correlates with a higher degree of intergranular failure in tempers T6 and T7.

Representative equivalent stress-strain curves, based on Equation (3) and the parameter values in Table 2, are shown in Figure 4 and Figure 5. Corresponding θ - R curves based on Equation (4) are also shown in these figures in order to analyse the work-hardening of the materials. The influence of artificial aging is emphasized in Figure 4, while the effect of the forming process is displayed in Figure 5. Figure 6 illustrates the two hardening terms and how they contribute to the work-hardening modulus as a function of plastic strain for the RR material in temper T6. It is evident that the work-hardening modulus is dominated by the first term about up to necking. Then there is an intermediate region where both terms are contributing to θ , and finally for large strains (stage IV) the second term governs the behaviour. The initial hardening modulus $\theta_1 + \theta_2$ is within $\mu/18$ and $\mu/11$ for the considered material and temper combinations, where μ is the shear modulus. These values are in good accord with those given by Kocks (1976) and Lloyd (2006).

As expected, temper T6x exhibits the lowest yield strength and the strongest work-hardening due to a lower density of hardening precipitates and a greater amount of atoms in solid solution. Temper T6 exhibits the highest overall flow stress and the work-hardening modulus is consistently lower than for the T6x temper. The most important feature of the T7 temper is the low work-hardening modulus at large strains compared with the two other tempers, which is also reflected by the relatively low values of the hardening modulus θ_2 , cf.

Table 2. At small strains, however, temper T7 displays strong work-hardening. The reason for the high work-hardening modulus at small strains is believed to be storage of geometrically necessary dislocations caused by non-shearable hardening precipitates. The low work-hardening modulus at large strains is linked to increased dynamic recovery compared with T6x and T6 tempers due to a lower amount of alloying elements in solid solution. Another interesting observation is the seemingly lower work-hardening modulus of the EX material at large strains compared with the CH and RR materials. The reason is most probably the strong cube texture exhibited by the EX material, while both the CH and RR materials are practically isotropic. Using crystal plasticity calculations, Khadyko (2015) found that the Taylor factor in uniaxial tension increases significantly at large strains for an aluminium alloy with random texture. The Taylor factor under uniaxial tension along the extrusion direction of an extruded AA6060 alloy with strong cube texture was found to be constant and initially about 20% lower than for random texture. The increase of the Taylor factor for random texture may explain the higher work-hardening modulus at large strains observed for the CH and RR materials.

5.3 Numerical results

The aim of the numerical study on the behaviour of the RR materials was twofold: I) to evaluate the accuracy of the Bridgman-correction used to estimate the equivalent stress-strain curves of the materials and II) to examine the notch-strengthening effect. From Figure 3 it seems that the notch-strengthening effect depends on the artificial aging; it is significantly stronger for tempers T6 and T7 than for temper T6x.

The yield stress and the constants of the two-term Voce hardening rule were taken from Table 2, while the initial void volume fraction f_0 was calibrated by trial and error to the available experimental data. A value of f_0 equal to 0.0075 was found to give good overall agreement with the stress-strain behaviour and failure of the smooth and notched specimens for all three tempers.

The experimental and numerical true stress-strain curves for the three tempers are compared in Figure 7. In the same manner as for the experimental tests, the true strain is calculated from the initial and current values of the minimum cross-section of the sample, $\varepsilon = \ln(A_0 / A)$, while the true stress is defined as force divided by current area, $\sigma = F / A$. To illustrate the strain localization within the neck or notch, the deformed configurations of the smooth and notched samples at two strain levels are provided in Figure 8 for the T6 temper. It

is evident that the plastic flow is more constrained in the notched sample than within the neck of the smooth sample. Based on Figure 7, the following three conclusions are drawn. Firstly, the results for the smooth samples show that the Bridgman-correction method for estimating the equivalent stress-strain curve is accurate for isotropic materials. Secondly, the notch-strengthening effect is accurately predicted for tempers T6x and T7, while it is somewhat overestimated for temper T6. Thus, it is reasonable to assume that the difference in notch-strengthening effect is a result of the difference in the work-hardening between the three tempers leading to different distributions of the plastic strain. Thirdly, the Gurson model estimates the failure strains of both the smooth and notched samples with reasonable accuracy, taking into account the simplicity of the approach.

In Figure 9, the stress triaxiality $\sigma^* = \sigma_H / \sigma_{eq}$ and the void volume fraction f in the critical element at the centre of the smooth and notched specimens are plotted against the true strain $\varepsilon = \ln(A_0 / A)$ over the minimum cross-section, where σ_H is the hydrostatic stress. The curves are plotted until f reaches 0.4. The void volume fraction increases exponentially with straining and the evolution depends strongly on the stress triaxiality. The work-hardening behaviour has significant impact on the stress-triaxiality level by modifying the plastic flow in the diffuse neck for the smooth specimen and in the notch for the notched specimen. This implies that the ductility of the different tempers, as determined from these tests, is indirectly influenced by the work-hardening behaviour: by lowering the work-hardening modulus for large strains, the stress triaxiality induced by the neck or notch increases, thus decreasing the ductility. This is important to bear in mind when evaluating the strain to failure in smooth and notched tensile tests. The highest and lowest stress triaxiality is found for the T7 and T6x tempers, respectively, that exhibited the strongest and weakest notch-strengthening effect. The drop in the critical element's stress triaxiality in the final part of the simulations of the notched samples is a result of the change of shape of the Gurson yield surface with the rapidly increasing void volume fraction. Figure 10 presents the simulated true stress-strain curves for the smooth and notched specimens in temper T6 together with the porosity evolution in the central element up to f equals 0.4. It is evident that failure is governed by the exponential void growth in the final part of the simulation which leads to a collapse of the yield surface. The results shown in the figure are not influenced by the element erosion that takes place at even higher levels of porosity.

5.4 Fracture

Scanning electron microscope (SEM) pictures of the global and local fracture surfaces of the smooth and notched samples are presented in Figure 11 and Figure 12 for the CH materials, in Figure 13 and Figure 14 for the EX materials and in Figure 15 and Figure 16 for the RR materials. In these figures, directions are only given for the anisotropic materials.

The global fracture surfaces are taken at low magnification to display the fracture mode, which is a kind of cup-and-cone mode for all samples; i.e., the shear mode that is sometimes observed for artificially aged aluminium alloys (Fourmeau et al., 2013) is not present. It is assumed that this is due to the relatively small grain size of the AA6060 materials. The fracture surface of the smooth and notched specimens for CH and RR materials have circular shape in all tempers, which is consistent with the nearly random texture measured for these materials. It is noted that the global fracture surface of the RR materials has a very rough appearance, which is even stronger for the notched specimens than for the smooth ones. The global fracture surface of the smooth specimens for the EX materials has an oval shape for all tempers, which is consistent with the strong cube texture exhibited by these materials. On the contrary, the shape of the global fracture surface of the notched specimens varies between the tempers. The shape is rhombic for temper T6x but circular for tempers T6 and T7. Again, the sharp cube texture combined with the superimposed triaxial stress field is responsible for the rhombic shape of the cross-section. Using the crystal plasticity finite element method to simulate tension tests on extruded and naturally aged AA6060 material, Khadyko et al. (2015) obtained the rhombic shape of the notched specimen's deformed cross-section when the strong cube texture was accounted for in the simulation. The reason for the circular shape in tempers T6 and T7 is probably the low failure strain, i.e., the specimen fails before the cube texture has been allowed to significantly change its shape, see Figure 3. It is important to note that the development of a rhombic shape of the minimum cross-section at large strain introduces uncertainties in the calculations of the current area, which is based on an elliptic shape of the cross-section (see Section 3.1). Accordingly, the true stress versus true strain curve obtained from the notched samples of the EX material in temper T6x is assumed less accurate for large strains.

The fracture surfaces are also investigated at higher magnification to reveal the fracture mechanisms. A high density of dimples with iron-rich primary particles observed at the bottom is found for all combinations of material and temper, indicating a ductile fracture mode involving nucleation, growth and coalescence of voids. In temper T6x, the fracture is mainly transcrystalline for all three materials, and the fracture mechanism is similar to that

found for the naturally aged AA6060 material (Pedersen et al., 2015). At peak hardness (temper T6), several areas of intercrystalline fracture are observed. These areas are even more pronounced for the notched specimens than for the smooth ones due to the increased stress triaxiality. As the material is overaged (temper T7), some areas of intercrystalline fracture are still seen but to lower degree than for temper T6. The intercrystalline fracture is assumed to be caused by the precipitation free zones formed adjacent to the grain boundaries in temper T6 and T7. It is well known that these zones are weaker than the interior of the grains. Strain will localize to the precipitation free zones and crack initiation and growth will more easily occur in these regions (see e.g. Dowling and Martin, 1976; Morgeneyer et al., 2008; Chen et al., 2009). The low fraction of intercrystalline fracture in these materials is caused by the small grain size, where the grain nodes are enforcing stress to the matrix preventing the fracture to occur along the grain boundaries (Lohne and Naess, 1979). Another factor that will contribute to intergranular failure is the amount of grain boundary precipitation (Chen et al, 2009), which has not been investigated here.

Figure 17 shows the failure strain plotted against the aging time for the three forming processes. The general trend is that the failure strain decreases with aging time, i.e., the ductility tends to decrease with increasing strength and decreasing work-hardening modulus at large strains. The exception is temper T7 of the EX material that has slightly better ductility than temper T6. It is interesting to note here that the work-hardening modulus in temper T6 is markedly lower for the EX material than for the CH and RR materials, see Figure 5. This difference in work-hardening behaviour may contribute to the relatively lower ductility in temper T6 for the EX material. In all cases, the underaged temper exhibits the superior ductility. It is further noted that the CH material displays the lowest ductility in all tempers, while the EX material has the highest overall ductility. The reason for this is most probably the large primary particles situated at the dendrite and grain boundaries of the CH material (Westermann et al., 2014). During the extrusion process, these particles are broken-up into smaller pieces and distributed more evenly, and the particles are now aligned in stringers along the EX direction (see also Figure 2).

6. Concluding remarks

The work-hardening and ductility of the AA6060 aluminium alloy were studied by tensile testing using smooth and notched samples. The alloy was subjected to three succeeding processing steps and thereafter artificially aged to underaged (T6x), peak aged (T6) and overaged (T7) conditions. The underaged temper was found to exhibit the strongest

work-hardening. Owing to the rather short aging time, a considerable amount of Mg and Si remain in solid solution, thus reducing the dynamic recovery and increasing the density of stored dislocations. The work-hardening of T6x temper was similar for all materials at low strains, but at large strains the EX material exhibited less work-hardening. The reason for this is assumed to be the strong cube texture of the EX material compared to the nearly random texture in the CH and RR materials. At peak hardness, temper T6, the work-hardening modulus is consistently lower than for the T6x temper due to the lower solute content. In the overaged condition, temper T7, the work-hardening modulus is high initially due to generation of geometrically necessary dislocations, but at large strain it is considerable lower than for the two other tempers. The latter is ascribed to the low solute level in the overaged temper, which will lead to an increased dynamic recovery rate compared with the other two tempers.

The study showed that the notch effect on the stress level and the failure strain was weaker in the underaged temper than in the peak aged and overaged tempers. This was attributed to the stronger work-hardening in the T6x condition that distributes plasticity over a larger region of the notch and reduces the geometrical constraint—and accordingly the stress triaxiality. The markedly lower ductility observed for the peak aged and overaged tempers was linked to a higher degree of intergranular fracture due to the existence of precipitate free zones along the grain boundaries. In addition, the numerical study with the Gurson model showed that the work hardening influences the stress triaxiality evolution in the neck or notch region, and thus indirectly affects the ductility of the material as a function of heat treatment. Previous studies have shown that the tensile ductility scales with the yield strength for the same microstructure, and thus also the higher yield strength of the peak aged and overaged tempers may in itself play a role for the ductility. The cast and homogenized material exhibited lower ductility than the extruded and the rolled and recrystallized materials. This was attributed to the breaking-up and redistribution of primary particles during the extrusion process.

Acknowledgement

The financial support from the Centres for Research-based Innovation SIMLab and CASA at the Norwegian University of Science and Technology (NTNU) is gratefully acknowledged.

References

- Ashby, M.F., 1970. The deformation of plastically non-homogeneous materials. *Philosophical Magazine* 21, 399–424.
- Benzerga, A.A., Leblond, J.-B., 2010. Ductile fracture by void growth to coalescence. *Advances in Applied Mechanics* 44, 169–305.
- Bridgman, P., 1944. The stress distribution at the neck of a tension specimen. *Transactions of the American Society for Metals* 32, 553–574.
- Chen, Y., Pedersen, K.O., Clausen, A.H., Hopperstad, O.S., 2009. An experimental study on the dynamic fracture of extruded AA6xxx and AA7xxx aluminium alloys. *Materials Science and Engineering A523*, 253–262.
- Cheng, L.M., Poole, P.W., Embury, J.D., Lloyd, D.J., 2003. The influence of precipitation on the work-hardening behavior of the aluminum alloys AA6111 and AA7030. *Metallurgical and Materials Transactions A* 34, 2473–2481.
- Chu, C., Needleman, A., 1980. Void nucleation effects in biaxially stretched sheets. *Journal of Engineering Materials and Technology* 102, 249–256.
- Dowling, J.M., Martin, J.W., 1976. The influence of MN additions on the deformation behaviour of an Al-Mg-Si alloy. *Acta Metallurgica* 24, 1147–1163.
- Dumont, D., Deschamps, A., Brechet, Y., 2003. On the relationship between microstructure, strength and toughness in AA7050 aluminum alloy. *Materials Science and Engineering A356*, 326–336.
- Embury, J.D., Poole, W.J., Lloyd, D.J., 2006. The work hardening of single phase and multi-phase aluminum alloys. *Materials Science Forum* 519-521, 71–78.
- Fourmeau, M., Børvik, T., Benallal, A., Hopperstad, O.S., 2013. Anisotropic failure modes of high-strength aluminium alloy under various stress states. *International Journal of Plasticity* 48, 34–53.
- Furu, T., Pedersen, K.O., 2006. The influence of grain structure and texture on formability and toughness of extruded aluminium alloys. *Materials Science Forum* 519-521, 1421–1428.
- Gurson, A.L., 1977. Continuum theory of ductile rupture by void nucleation and growth: Part I – Yield criteria and flow rules for porous ductile media. *Journal of Engineering Materials and Technology* 99, 2–15.

- Johnsen, J., Holmen, J.K., Myhr, O.R., Hopperstad, O.S., Børvik, T., 2013. A nano-scale material model applied in finite element analysis of aluminium plates under impact loading. *Computational Materials Science* 79, 724–735.
- Khadyko, M., Dumoulin, S., Børvik, T., Hopperstad, O.S., 2014. An experimental-numerical method to determine the work-hardening of anisotropic ductile materials at large strains. *International Journal of Mechanical Sciences* 88, 25–36.
- Khadyko, M., Dumoulin, S., Børvik, T., Hopperstad, O.S., 2015. Simulation of large-strain behaviour of AA6060 under tensile loading using anisotropic plasticity models. *Computers and Structures* 157, 60–75.
- Khadyko, M., 2015. Experimental and numerical study of yielding, work-hardening and anisotropy in textured AA6xxx alloys using crystal plasticity models. Doctoral thesis 2015:28. Norwegian University of Science and Technology, Trondheim, Norway.
- Kocks, U.F., 1976. Laws for work-hardening and low-temperature creep. *Journal of Engineering Materials and Technology, Transactions of the ASME*, 76–85.
- Le Roy, G., Embury, J.D., Edwards, G., Ashby, M.F., 1981. A model of ductile fracture based on the nucleation and growth of voids. *Acta Metallurgica* 29, 1509–1522.
- Liu, G., Scudino, S., Li, R., Kühn, U., Sun, J., Eckert, J., 2011. Coupling effect of primary voids and secondary voids on the ductile fracture of heat-treatable aluminum alloys. *Mechanics of Materials* 43, 556–566.
- Lloyd, D.J., 2003. The scaling of the tensile ductile fracture strain with yield strength in Al alloys. *Scripta Materialia* 48, 341–344.
- Lloyd, D.J., 2006. The work hardening of some commercial alloys. *Materials Science Forum* 519-521, 55–62.
- Lohne, O., Naess, O.J., 1979. The effects of dispersoids and grain size on mechanical properties of AlMgSi alloys. *Proceedings of the 5th International Conference of Strength of Metals and Alloys, Aachen*, 781–788.
- Maire, E., Zhou, S., Adrien, J., Dimichiel, M., 2011. Damage quantification in aluminium alloys using in situ tensile tests in X-ray tomography. *Engineering Fracture Mechanics* 78, 2679–2690.
- Morgeneyer, T.F., Starink, M.J., Wang, S.C., Sinclair, I., 2008. Quench sensitivity of toughness in an Al alloy: Direct observation and analysis of failure initiation at the precipitate-free zone. *Acta Materialia* 56, 2872–2884.

- Myhr, O.R., Grong, Ø., Pedersen, K.O., 2010. A combined precipitation, yield strength, and work hardening model for Al-Mg-Si alloys. *Metallurgical and Materials Transactions A* 41, 2276–2289.
- Nahshon K, Hutchinson J.W. Modification of the Gurson model for shear failure. *European Journal of Mechanics A/Solids* 2008;27:1–17.
- Pedersen, K.O., Westermann, I., Furu, T., Børvik, T., Hopperstad, O.S., 2015. Influence of microstructure on the work-hardening and ductile fracture of aluminium alloys. *Materials and Design* 70, 31–44
- Teirlinck, D., Zok, F., Embury, J.D., Ashby, M.F., 1988. Fracture mechanism maps in stress space. *Acta Metallurgica* 36, 1213–28.
- Toda, H., Oogo, H., Horikawa, K., Uesugi, K., Takeuchi, A., Suzuki, Y., Nakazawa, M., Aoki, Y., Kobayashi, M., 2014. The true origin of ductile fracture in aluminum alloys. *Metallurgical and Materials Transactions* 45A, 765–776.
- Tvergaard, V., 1981. Influence of voids on shear band instabilities under plane strain conditions. *International Journal of Fracture* 17, 389–407.
- Tvergaard, V., Needleman, A., 1984. Analysis of the cup-cone fracture in a round tensile bar. *Acta Metallurgica* 32, 157–169.
- Westermann, I., Pedersen, K.O., Furu, T., Børvik, T., Hopperstad, O.S., 2014. Effects of particles and solutes on strength, work-hardening and ductile fracture of aluminium alloys. *Mechanics of Materials* 79, 58–72.
- Xue, Z., Pontin, M.G., Zok, F.W., Hutchinson, J.W., 2010. Calibration procedures for a computational model of ductile fracture. *Engineering Fracture Mechanics* 77, 492–509.

List of tables:

Table 1: Mechanical data from typical tests for the three materials and four temper conditions.

Table 2: Work-hardening parameters for the three materials and four temper conditions.

List of figures:

Figure 1. Sketch of material processing steps after casting: homogenization, extrusion, and rolling and recrystallization (from Pedersen et al., 2015).

Figure 2: Grain structure, constituent particle structure and orientation distribution function for the AA6060 material after the three subsequent processing steps (from Pedersen et al., 2015).

Figure 3: True stress versus true strain curves for smooth (S) and notched (N) samples of the CH, EX and RR materials (left to right) in tempers T6x, T6 and T7 (top to bottom). It is noted that the stress-strain curves for the EX material in temper T6x are uncertain because the cross-section developed a diamond shape at large strains (see Figure 13).

Figure 4: Representative equivalent stress-strain curves and corresponding θ - R curves for all tempers: (a) CH, (b) EX and (c) RR materials.

Figure 5: Representative equivalent stress-strain curves and corresponding θ - R curves for all materials: (a) T6x, (b) T6 and (c) T7 temper.

Figure 6: Illustration of the two hardening terms and how they contribute to the work-hardening modulus as a function of plastic strain for the RR material in temper T6.

Figure 7: True stress versus true strain curves from experiments and simulations with the Gurson model for smooth (S) and notched (N) samples of the RR material in (a) temper T6x, (b) temper T6 and (c) temper T7.

Figure 8: Colour plots of the effective plastic strain distribution over the minimum cross-section at two different strain levels in a) smooth and b) notched specimen from FE simulations of the RR material in temper T6. The fringe range in a) is from 0 (blue) to 1 (red), while the fringe range in b) is from 0 (blue) to 0.5 (red).

Figure 9: Results from simulations with the Gurson model of the smooth and notched samples of the RR materials in temper T6: a) Stress triaxiality and b) void volume fraction f in the critical element versus true strain $\varepsilon = \ln(A_0 / A)$ over the minimum cross-section.

Figure 10: Results from simulations with the Gurson model of the smooth and notched samples of the RR materials in temper T6: true stress-strain curves with evolution of void volume fraction in the critical element superimposed.

Figure 11: Global fracture surfaces of smooth and notched CH samples.

Figure 12: Local fracture surfaces of smooth and notched CH samples.

Figure 13: Global fracture surfaces of smooth and notched EX samples.

Figure 14: Local fracture surfaces of smooth and notched EX samples.

Figure 15: Global fracture surfaces of smooth and notched RR samples.

Figure 16: Local fracture surfaces of smooth and notched RR samples.

Figure 17: Failure strain versus aging time in hours from tensile tests on smooth cylindrical specimens.

Tables:

Table 1: Mechanical data from typical tests for the three materials and four temper conditions.

Material- temper	$\sigma_{0.2}$ [MPa]	σ_u [MPa]	ε_u [-]	σ_f [MPa]	ε_f [-]
CH-T6x	97.3	185.4	0.25	329.2	0.84
CH-T6	174.0	223.3	0.13	347.8	0.69
CH-T7	191.0	220.8	0.08	291.7	0.52
EX-T6x	99.2	181.5	0.15	325.5	1.31
EX-T6	192.0	235.9	0.09	354.6	0.89
EX-T7	172.7	206.3	0.07	290.8	0.95
RR-T6x	97.2	183.7	0.24	330.0	1.03
RR-T6	180.0	227.7	0.12	378.0	0.86
RR-T7	174.5	208.1	0.08	309.7	0.82

Table 2: Work-hardening parameters for the three materials and four temper conditions.

Material- temper	σ_0 [MPa]	Q_1 [MPa]	C_1 [-]	θ_1 [MPa]	Q_2 [MPa]	C_2 [-]	θ_2 [MPa]
CH-T6x	99.0	79.8	21.1	1684	120.4	2.57	309.4
CH-T6	175.0	64.3	24.0	1543	115.5	1.27	146.7
CH-T7	193.4	42.3	35.5	1502	77.1	0.87	67.1
EX-T6x	97.2	107.3	21.0	2253	83.6	0.90	75.2
EX-T6	202.6	53.3	26.2	1396	85.2	0.77	65.6
EX-T7	170.8	50.8	39.6	2012	55.7	0.49	27.3
RR-T6x	98.8	85.3	18.5	1578	99.8	2.69	268.5
RR-T6	180.5	65.6	23.4	1535	129.9	0.99	128.6
RR-T7	173.7	47.9	38.1	1825	105.6	0.60	63.4

Figures:

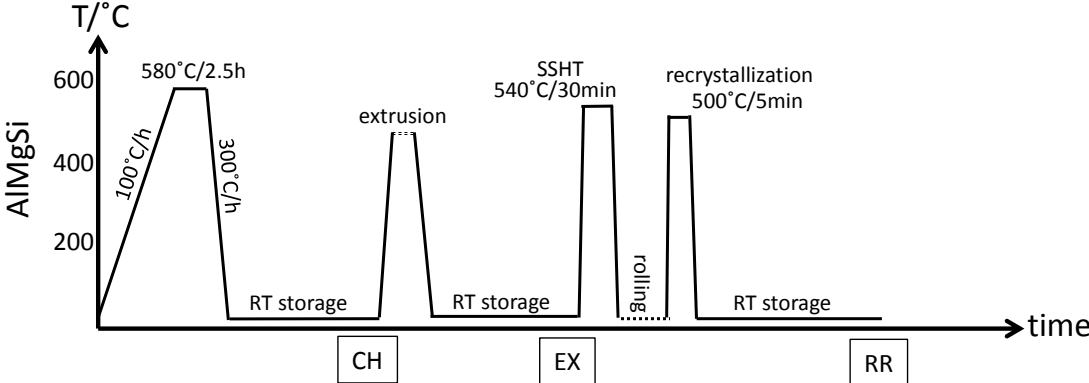


Figure 1. Sketch of material processing steps after casting: homogenization, extrusion, and rolling and recrystallization (from Pedersen et al., 2015).

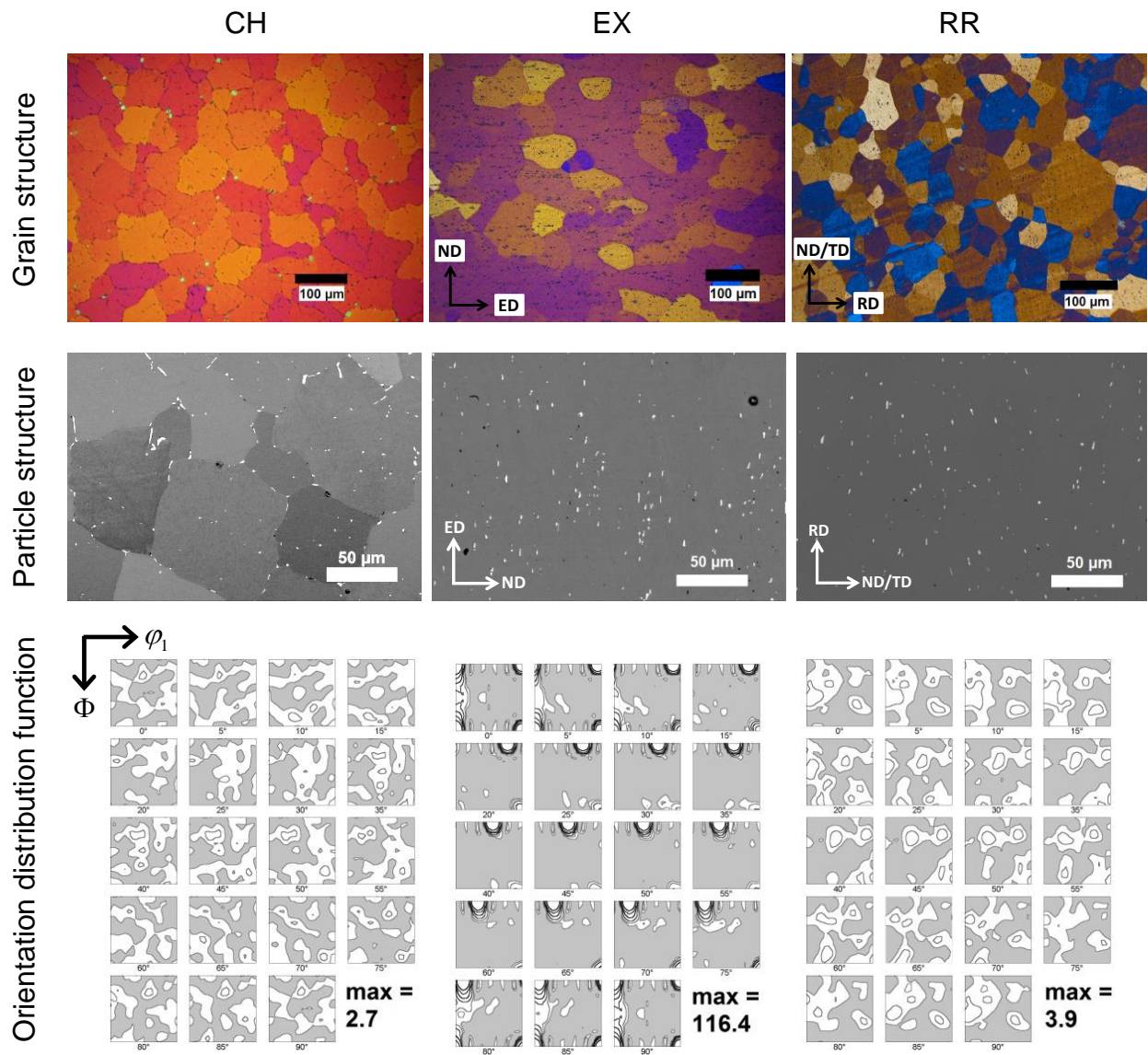


Figure 2: Grain structure, constituent particle structure and orientation distribution function for the AA6060 material after the three subsequent processing steps (from Pedersen et al., 2015).

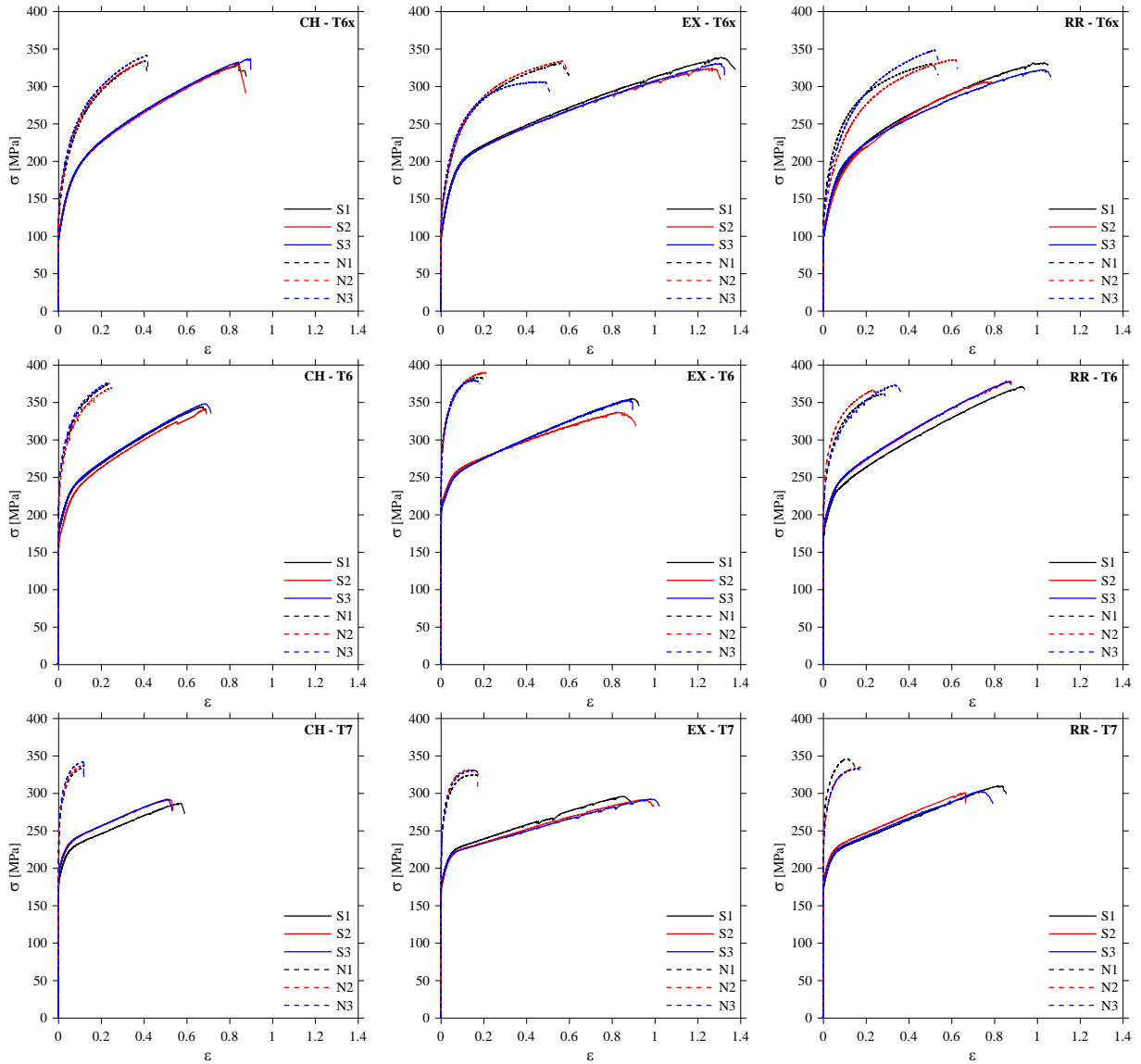


Figure 3: True stress versus true strain curves for smooth (S) and notched (N) samples of the CH, EX and RR materials (left to right) in tempers T6x, T6 and T7 (top to bottom). It is noted that the stress-strain curves for the EX material in temper T6x are uncertain because the cross-section developed a diamond shape at large strains (see Figure 13).

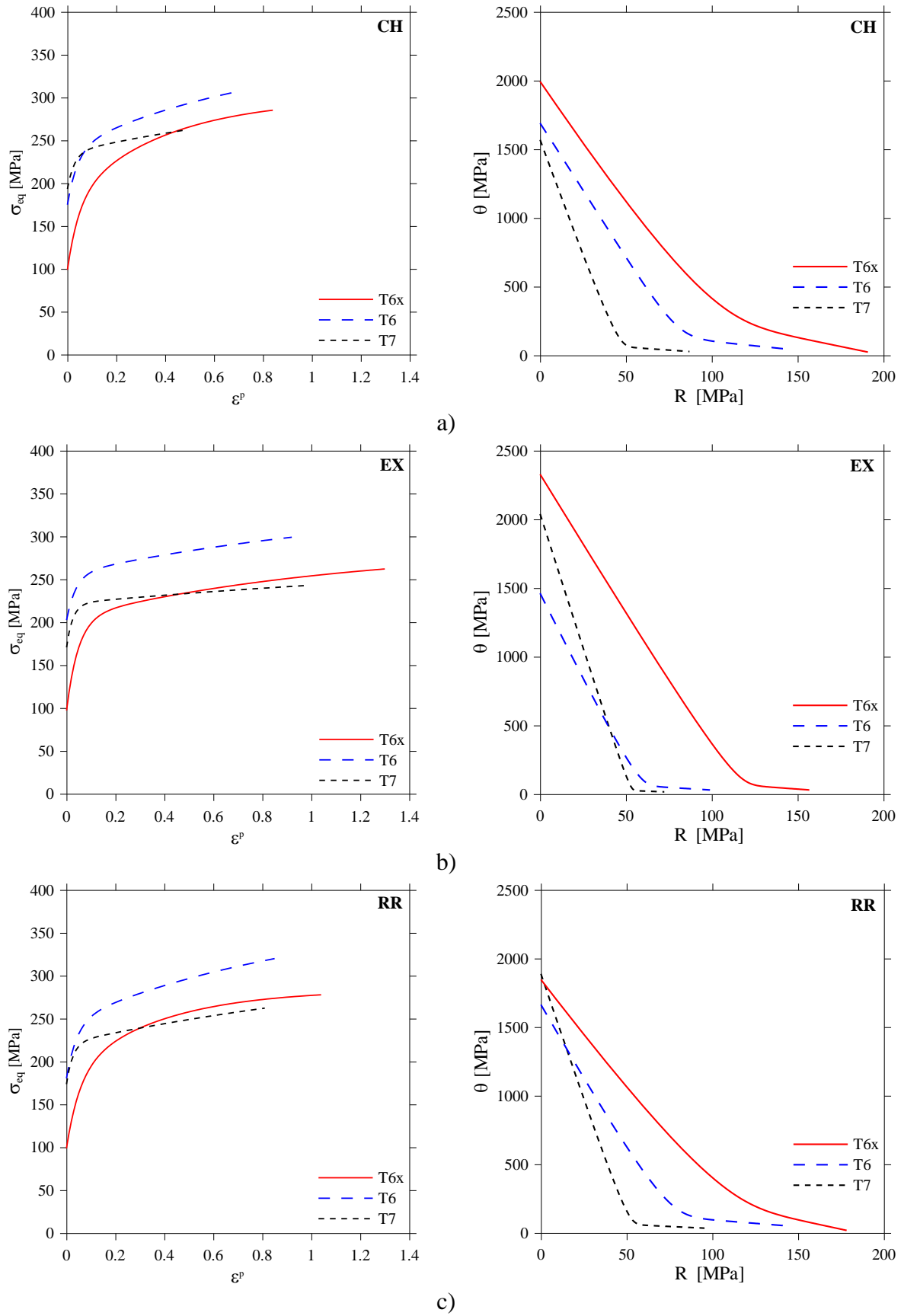


Figure 4: Representative equivalent stress-strain curves and corresponding θ - R curves for all tempers: (a) CH, (b) EX and (c) RR materials. Note that the results for the EX material is based on the Bridgman correction even though the material exhibited plastic anisotropy.

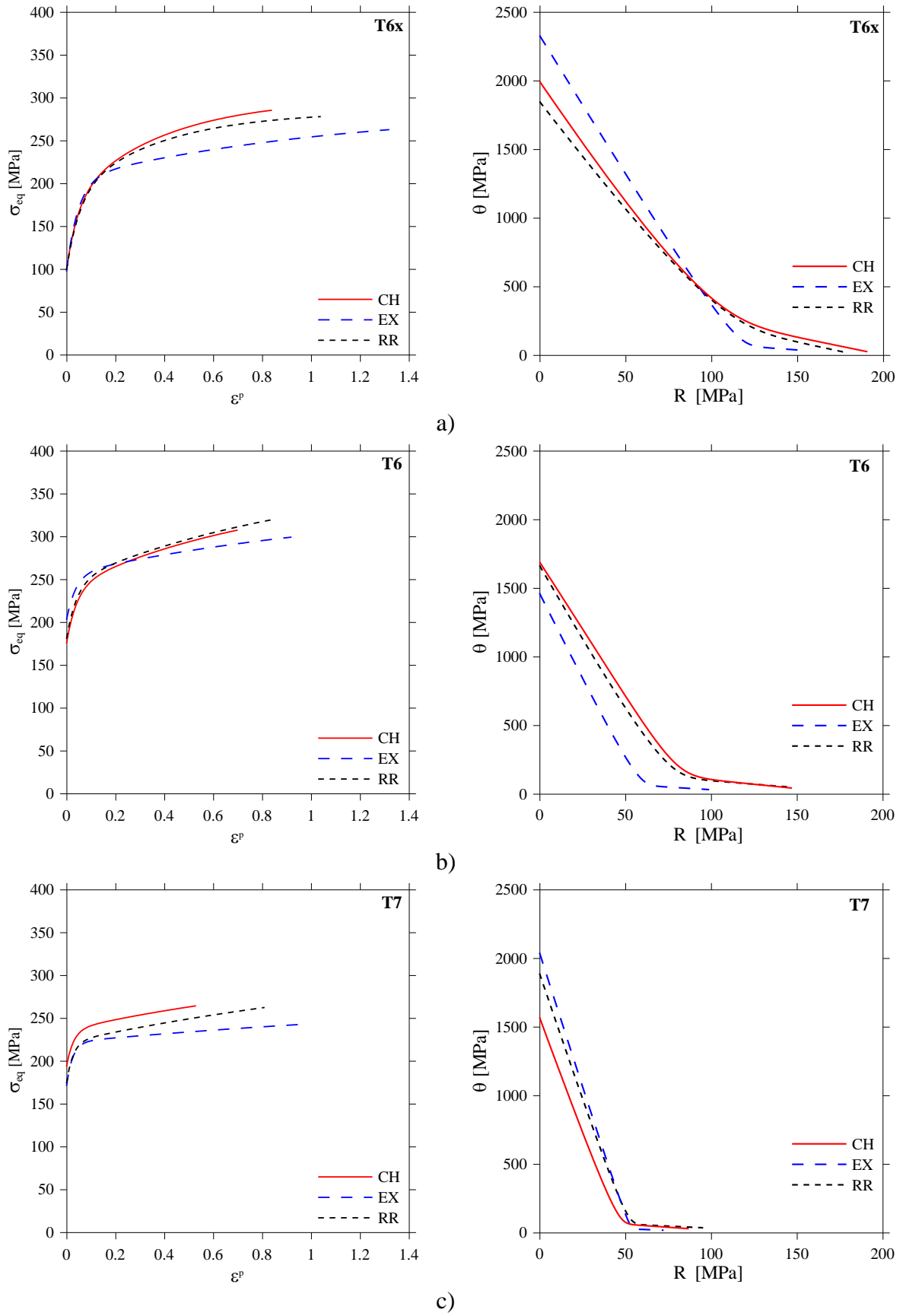


Figure 5: Representative equivalent stress-strain curves and corresponding θ - R curves for all materials: (a) T6x, (b) T6 and (c) T7 temper. Note that the results for the EX material is based on the Bridgman correction even though the material exhibited plastic anisotropy.

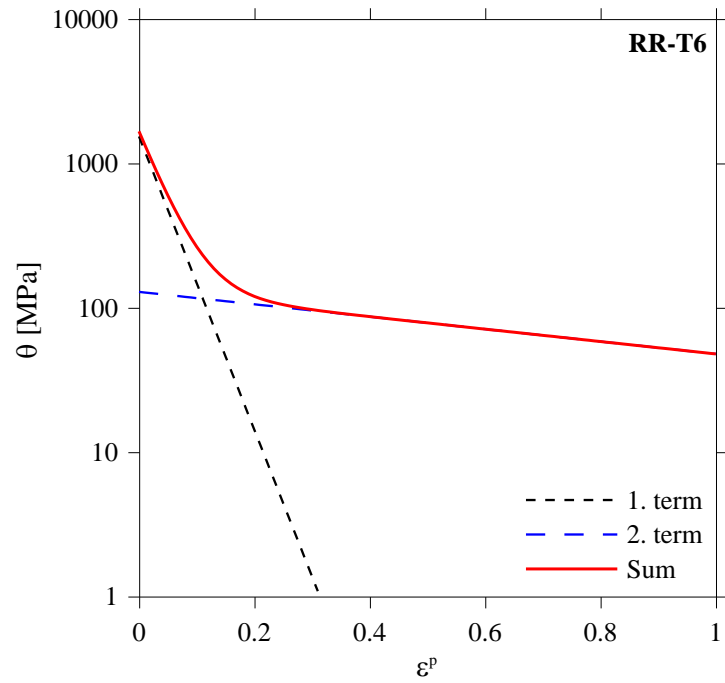


Figure 6: Illustration of the two hardening terms and how they contribute to the work-hardening modulus as a function of plastic strain for the RR material in temper T6.

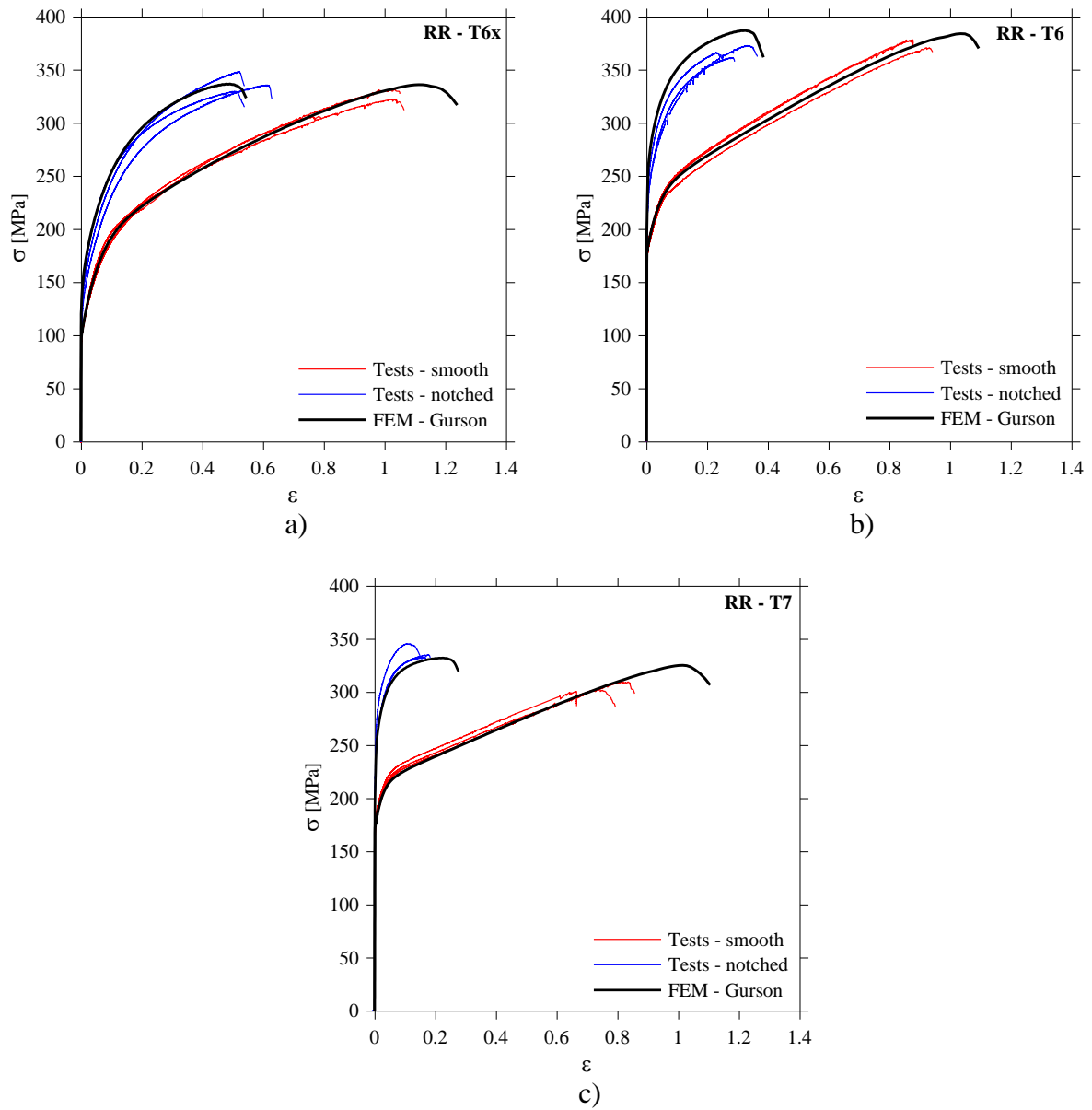


Figure 7: True stress versus true strain curves from experiments and simulations with the Gurson model for smooth (S) and notched (N) samples of the RR material in (a) temper T6x, (b) temper T6 and (c) temper T7.

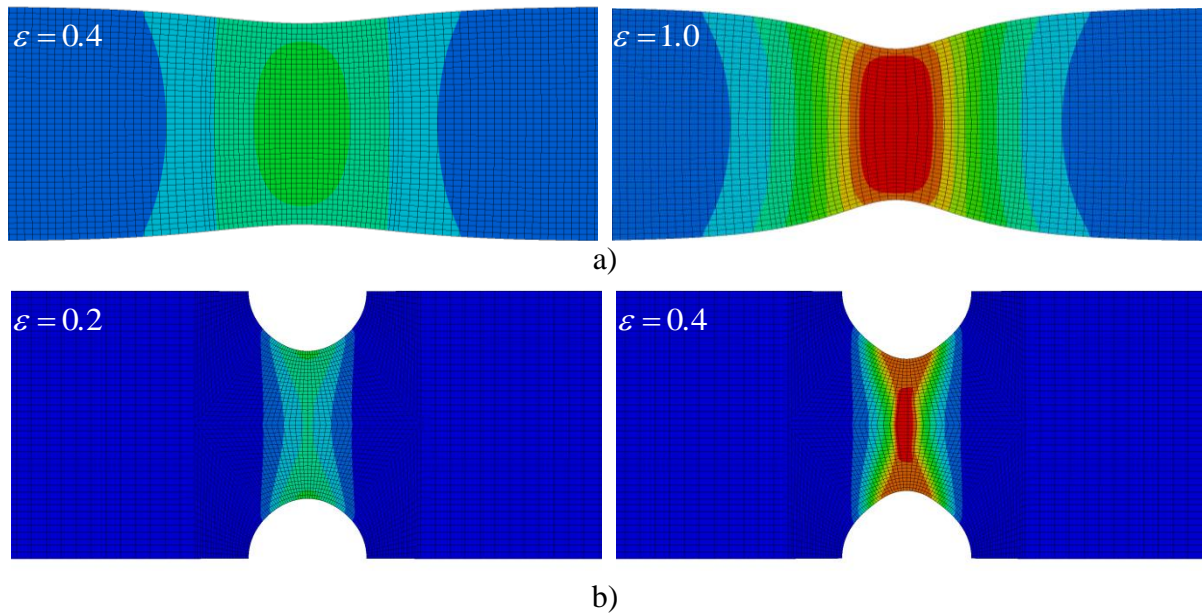


Figure 8: Colour plots of the effective plastic strain distribution over the minimum cross-section at two different strain levels in a) smooth and b) notched specimen from FE simulations of the RR material in temper T6. The fringe range in a) is from 0 (blue) to 1 (red), while the fringe range in b) is from 0 (blue) to 0.5 (red).

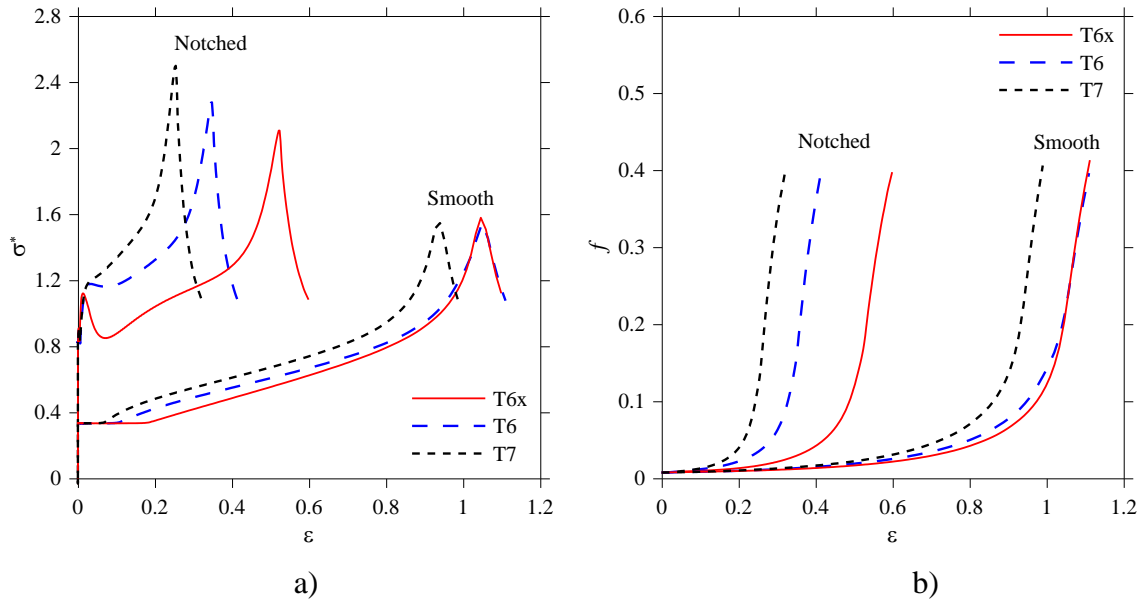


Figure 9: Results from simulations with the Gurson model of the smooth and notched samples of the RR materials in temper T6: a) Stress triaxiality σ^* and b) void volume fraction f in the critical element versus true strain $\epsilon = \ln(A_0 / A)$ over the minimum cross-section.

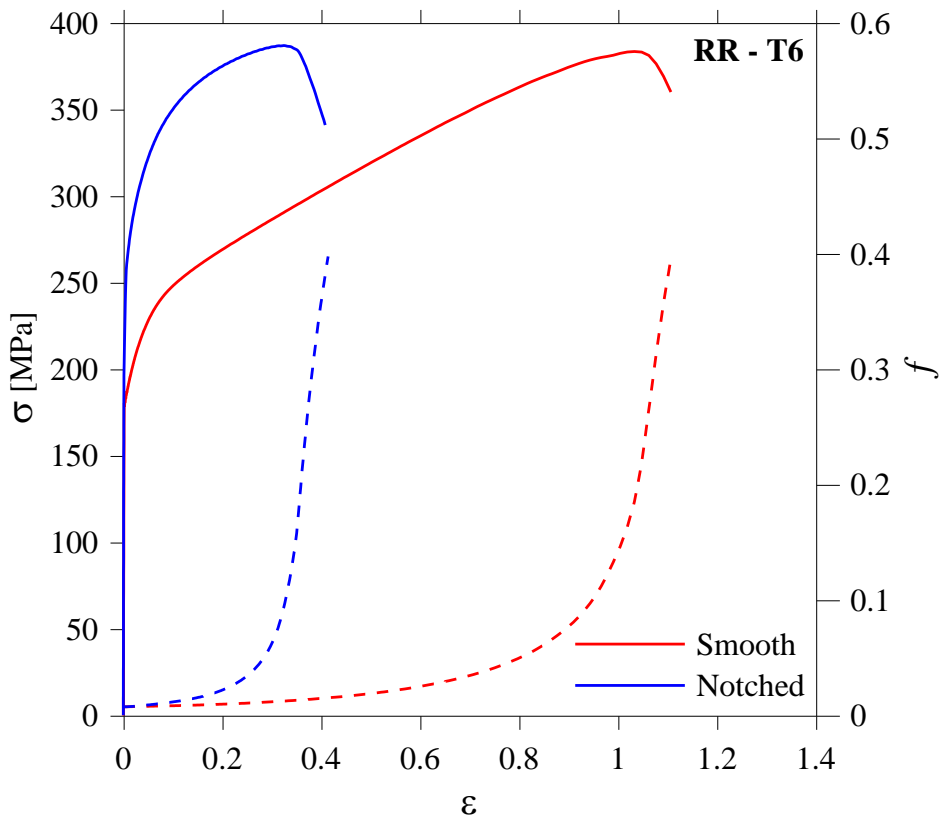


Figure 10: Results from simulations with the Gurson model of the smooth and notched samples of the RR materials in temper T6: true stress-strain curves with evolution of void volume fraction in the critical element superimposed.

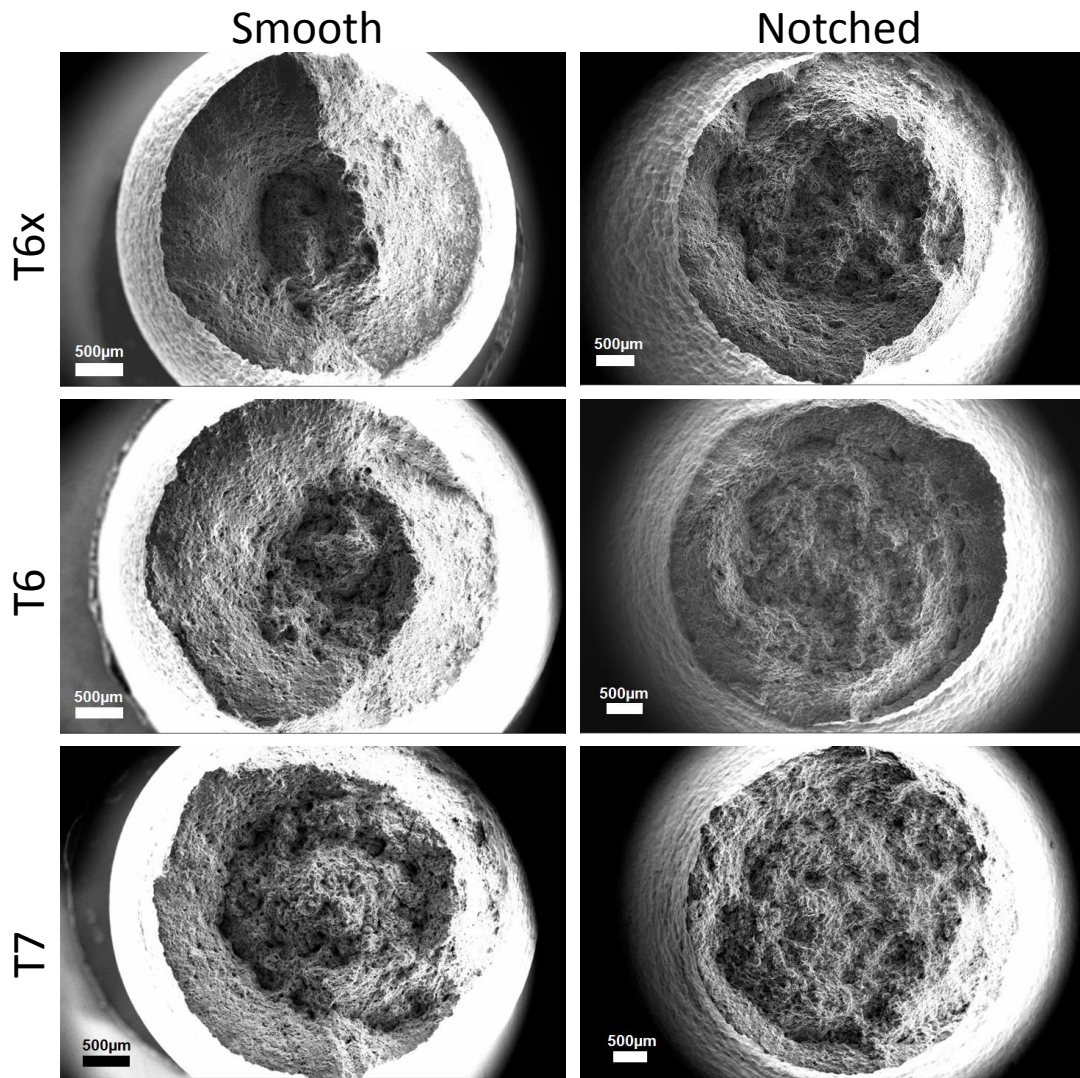


Figure 11: Global fracture surfaces of smooth and notched CH samples.

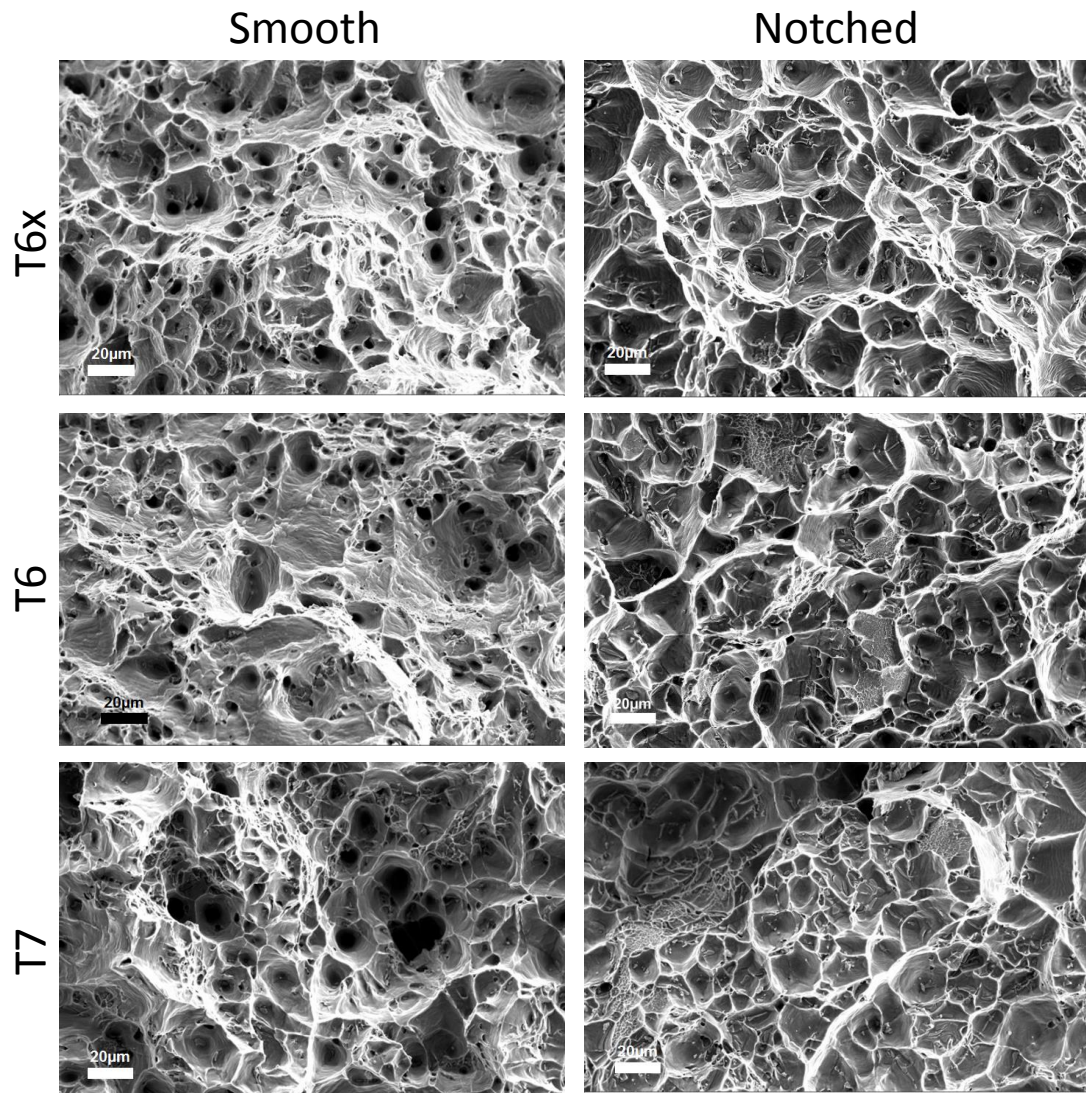


Figure 12: Local fracture surfaces of smooth and notched CH samples.

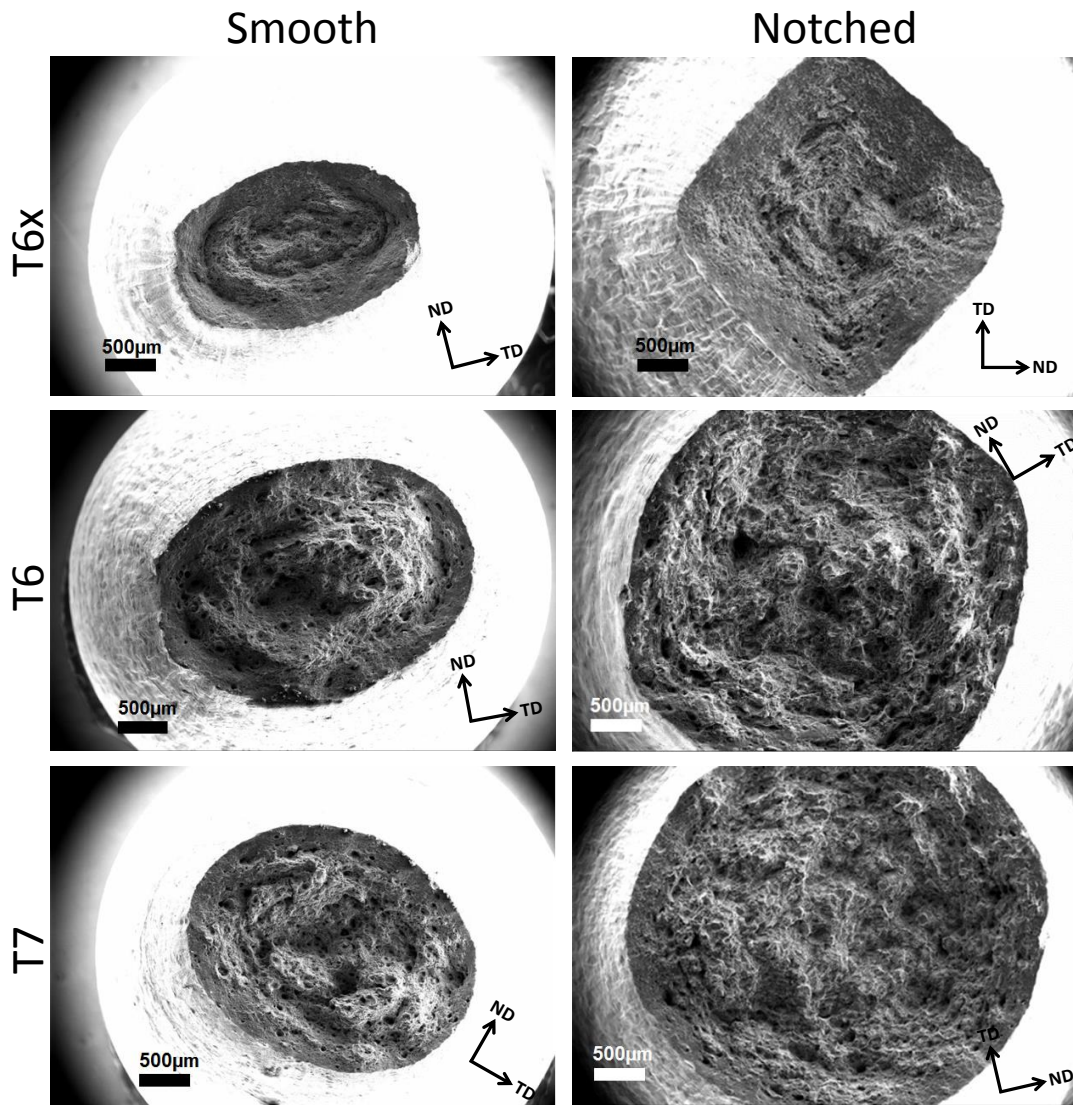


Figure 13: Global fracture surfaces of smooth and notched EX samples.

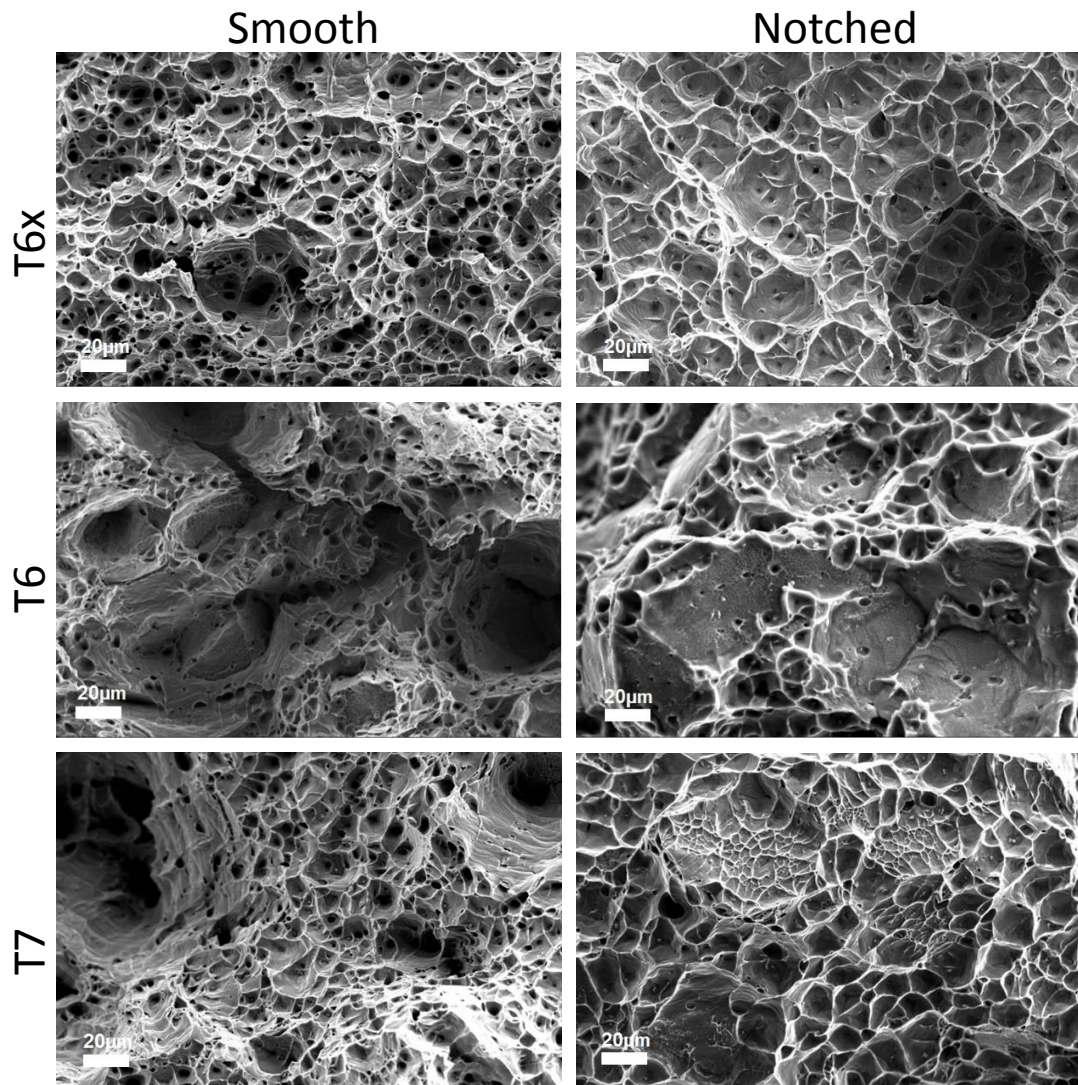


Figure 14: Local fracture surfaces of smooth and notched EX samples.

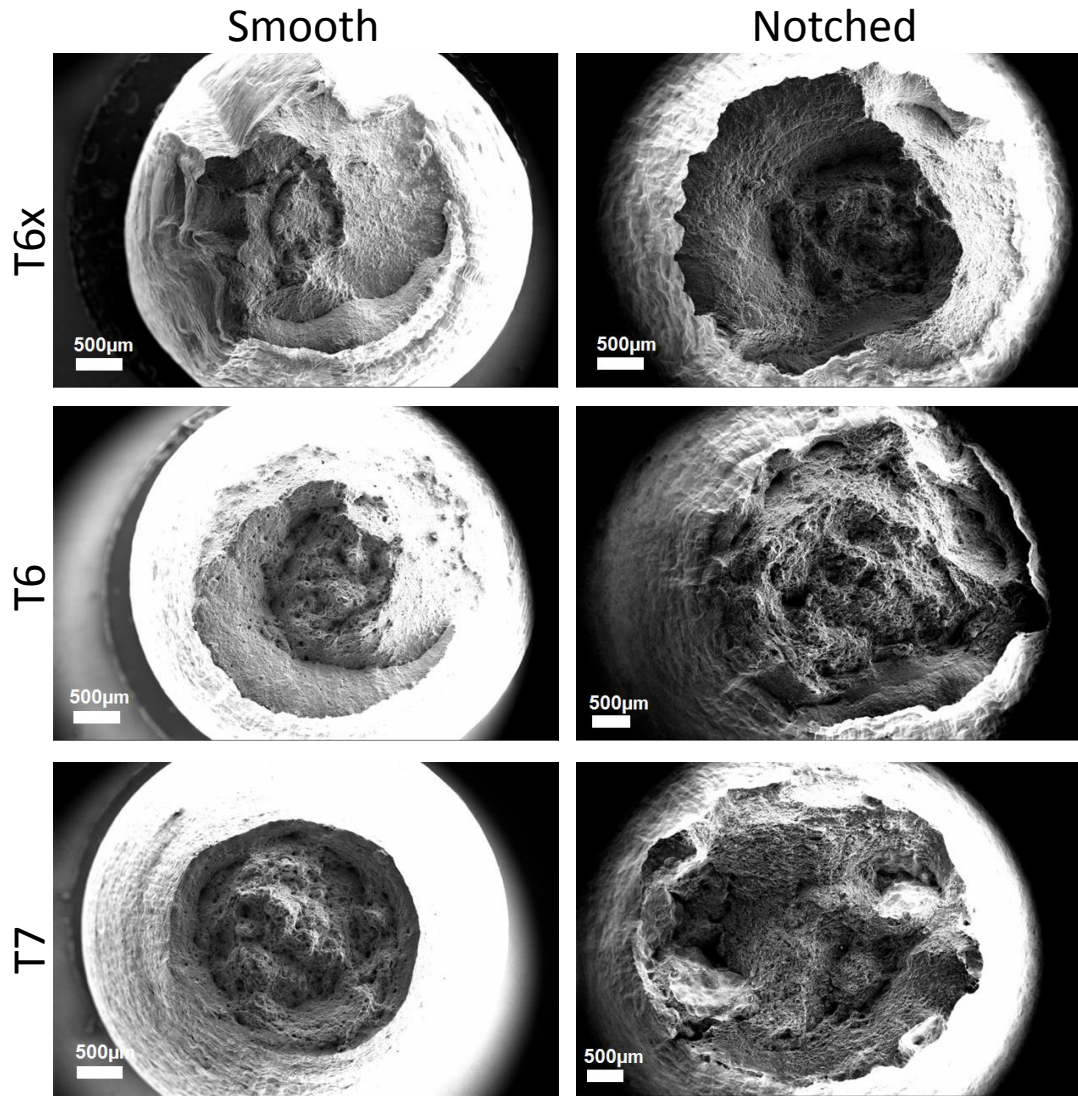


Figure 15: Global fracture surfaces of smooth and notched RR samples.

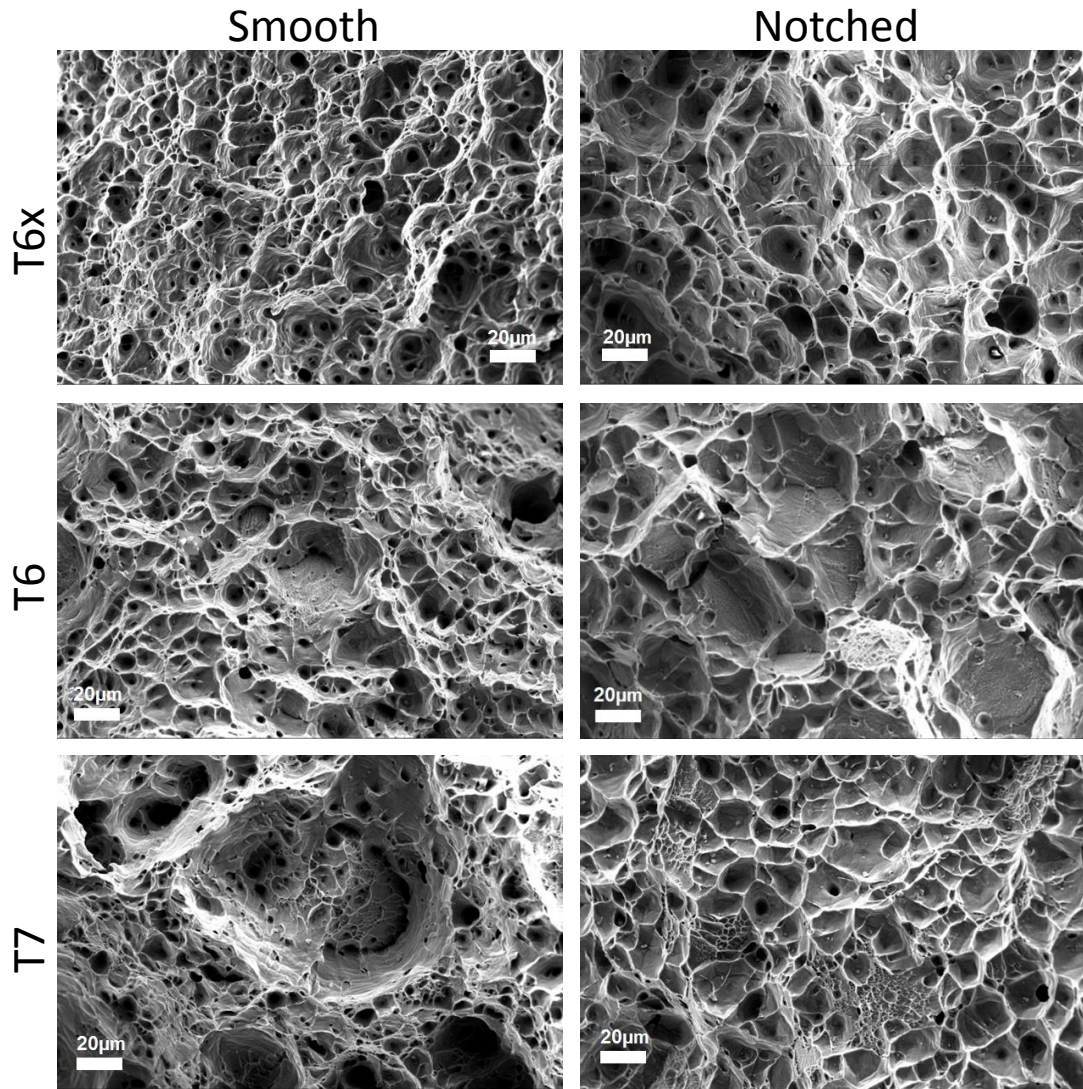


Figure 16: Local fracture surfaces of smooth and notched RR samples.

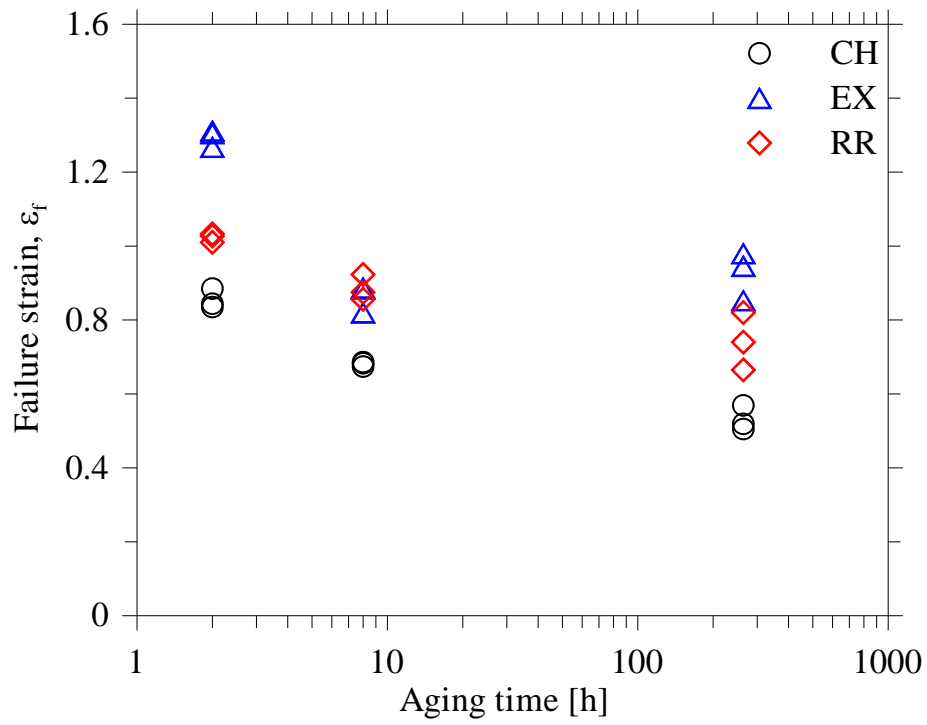


Figure 17: Failure strain versus aging time in hours from tensile tests on smooth cylindrical specimens.